APPLIED ORGANOMETALLIC CHEMISTRY
Appl. Organometal. Chem. 2005; **19**: 1015–1021
Materials, Nanoscience and Catalysis AOC
Published online 29 July 2005 in Wiley InterScience (www.interscience.wiley.com). DOI:10.1002/aoc.951

Infrared laser synthesis and properties of magnetic nano-iron–polyoxocarbosilane composites

Josef Pola[1]*, Miroslav Maryško[2], Vladimír Vorlíček[2], Zdeněk Bastl[3], Anna Galíková[1], Karel Vacek[1], Rodica Alexandrescu[4], Florian Dumitrache[4], Ion Morjan[4], Lavinia Albu[4] and Gabriel Prodan[5]**

[1]Laboratory of Laser Chemistry, Institute of Chemical Process Fundamentals, Academy of Sciences of the Czech Republic, 16502 Prague 6, Czech Republic
[2]Institute of Physics, Academy of Sciences of the Czech Republic, 18040 Prague, Czech Republic
[3]J. Heyrovsky Institute of Physical Chemistry, Academy of Sciences of the Czech Republic, 18223 Prague 8, Czech Republic
[4]National Institute for Lasers, Plasma and Radiation Physics, PO Box MG-36, R-76900 Bucharest, Romania
[5]Ovidius University of Constanta, POB 8600, Constanta, Romania

Received 22 March 2005; Accepted 11 May 2005

Nano-magnetic, thermally stable iron-based composites were obtained by a one-step procedure consisting of continuous-wave infrared laser-induced and ethylene-sensitized co-pyrolysis of gaseous iron pentacarbonyl and hexamethyldisiloxane in argon. The simultaneously occurring formation of iron from iron pentacarbonyl and that of organosilicon polymer from hexamethyldisiloxane yield iron nanoparticles surrounded by an organosilicon polymer shell. The particles were characterized by spectral analyses, electron microscopy, thermal gravimetry and magnetic measurements. They become superficially oxidized in the atmosphere. Their composition, thermal behaviour and magnetic properties depend on the flow rates of the precursors and the total pressure of the procedure. Magnetization curves, exchange bias H_{ex} at $T = 5$ K and AC susceptibility were studied in the temperature range 5–400 K. The values of H_{ex} verified the observed degree of the particle surface oxidation. The system of the iron nanoparticles is in a ferromagnetic blocked state and the temperature dependence of the coercivity and susceptibility is in accord with the transmission electron microscopy data.

KEYWORDS: laser-induced co-pyrolysis; iron pentacarbonyl; hexamethyldisiloxane; iron–iron oxide/polyoxocarbosilane nanocomposite; magnetic and thermal properties

INTRODUCTION

Nanocomposite magnetic materials[1] with magnetic species separated by the use of a non-magnetic matrix (e.g. silicon oxides,[2] mesoporous silica,[3] porous glass[4] and various polymers[5–9]) have attracted a lot of recent attention owing to their promising applications in nanoscience and medicine.

*Correspondence to: Josef Pola, Laboratory of Laser Chemistry, Institute of Chemical Process Fundamentals, Academy of Sciences of the Czech Republic, 16502 Prague 6, Czech Republic.
E-mail: pola@icpf.cas.cz
**Correspondence to: Rodica Alexandrescu, National Institute of Lasers, Plasma and Radiation Physics, PO Box MG-36, R-76900 Bucharest, Romania.
E-mail: rodica.alexandrescu@inflpr.ro
Contract/grant sponsor: NATO; Contract/grant number: CLG 980587.

The incorporation of nanomagnetic particles of iron oxide in organic polymers was achieved through static casting,[10] a wet chemical approach,[11] ultrasound radiation,[12] *in situ* oxidation of iron salts within polymer latex,[13] seed precipitation polymerization in the presence of iron oxide nanoparticles[14] and also by laser vaporization of metals into ultrafine metal and cationic particles that act as polymerization catalysts.[15] Nanomagnetic particles of iron stabilized by polymers have been prepared by sonolysis of iron pentacarbonyl in the presence of poly(dimethylphenyleneoxide).[16]

Another approach to these materials is infrared (IR) laser irradiation of gaseous mixtures of two volatile compounds, which of one serves as a precursor of iron and the other as a precursor of a polymer. This procedure was recently documented via IR laser-induced and ethylene-sensitized co-pyrolysis of iron pentacarbonyl and

methoxytrimethylsilane.[17] The concurrent decomposition of iron pentacarbonyl into iron and carbon monoxide and that of the organosilane into methylmethoxysilicone resulted in the formation of nanosized iron-based particles covered with organosilicon polymer.

Here, we further exploit this technique by applying it to a mixture of iron pentacarbonyl and hexamethyldisiloxane. We describe the spectral, thermal and magnetic properties of the nanocomposites produced, revealing that these observations are dependent on the flow rates of both precursors and the total pressure of the procedure.

EXPERIMENTAL

The IR laser irradiation of gaseous iron pentacarbonyl and hexamethyldisiloxane was conducted as described previously,[17] in a flow reactor equipped with NaCl windows and a continuous-wave (CW) CO_2 laser. Briefly, the vapours of iron pentacarbonyl and hexamethyldisiloxane (each diluted with ethene) together with argon (needed for gas and particle confinement) were introduced separately into the reaction chamber through three concentric nozzles at two different flow rates of $Fe(CO)_5$–C_2H_4 and $[(CH_3)_3Si]_2O$–C_2H_4 and two different total pressures (Table 1). The gas flows and the total pressure were independently controlled by electronic valves. The laser beam (output power 80 W, $\lambda = 10.6$ μm) was mildly focused by an NaCl lens to achieve an energy density of 2 kW cm^{-2} when crossed with the reactant flow. These conditions yielded at least 1 g of an ultrafine black powder after 1 h irradiation.

The black ultrafine powder obtained was transferred for measurements of its properties by Fourier transform IR (FTIR), Raman, electron paramagnetic resonance (EPR) and X-ray photoelectron spectroscopies and by electron microscopy and thermal gravimetry.

The FTIR spectra were obtained on powder in KBr pellets using a Nicolet Impact 400 spectrometer. The Raman spectra were recorded on a Renishaw (Ramascope model 1000) Raman microscope coupled with a CCD detector. The excitation beam of an argon-ion laser was defocused to obtain an energy density lower than 9×10^4 W cm^{-2} and to diminish the heating of the sample. The EPR spectra were registered on a CW X-band spectrometer with 100 kHz magnetic field modulation at room temperature and in the presence of air.

Table 1. Experimental conditions of laser irradiation

Run	Flow rate (sccm) C_2H_4[a]	$Fe(CO)_5$	C_2H_4[b]	$[(CH_3)_3Si]_2O$	P_{total} (mbar)
1	60	4.67	30	0.95	650
2	60	7.00	30	1.39	450

[a] Used for dilution of $Fe(CO)_5$.
[b] Used for dilution of $[(CH_3)_3Si]_2O$.

Transmission electron microscopy (TEM) photomicrographs on samples were recorded using a Philips 201 and a CM 120 transmission electron microscope. X-ray photoelectron spectroscopy (XPS) data were obtained with a Gammadata Scienta ESCA 310 electron spectrometer using monochromatized Al Kα ($h\nu = 1486.6$ eV) radiation for electron excitation. The energy scale of the spectrometer was calibrated with Au $4f_{7/2}$ binding energy fixed at 84.0 eV. The high-resolution spectra of Fe 2p, Si 2p, C 1s and O 1s photoelectrons were measured for an as-received sample and after mild argon-ion sputtering ($E = 5$ keV, $I = 40$ μA, $t = 5$ min). The ratios of atomic elemental concentrations were calculated assuming a homogeneous sample.

Thermogravimetric analysis of the solid deposit (sample weight 24 mg) was carried out by heating the sample up to 700 °C at a rate of 4 °C min^{-1}, using Cahn D-200 recording microbalances in a stream of argon.

Magnetization studies on the powder samples were performed in the temperature range 5–400 K using a SQUID magnetometer (MPMS-5S, Quantum Design). The AC susceptibility in a zero static magnetic field was measured at a frequency of 0.3 Hz with the exciting AC magnetic field set at 3.9 Oe.

Iron pentacarbonyl, hexamethyldisiloxane, ethene and argon (purity 99.9%) were purchased from Aldrich.

RESULTS AND DISCUSSION

CW CO_2 laser irradiation of the flow of hexamethyldisiloxane–iron pentacarbonyl–ethylene–argon mixtures results in efficient absorption of the laser radiation and heating of the mixture. The visible luminescence (flame) observed in a limited volume near the intersection of the laser beam with the inlet gas flow confirms the occurrence of electronically excited states. The laser decomposition of both hexamethyldisiloxane and iron pentacarbonyl is chiefly based on the excitation of ethylene (IR photosensitizer[18]) and a collisional energy transfer between the excited ethylene and these compounds. It takes place in a small and well-confined irradiation volume and results in the formation of gaseous products and black ultrafine powders. The CO_2 laser decomposition of both components was studied: that of $Fe(CO)_5$ results[19–23] in the formation of elemental iron along with carbon monoxide, whereas that of hexamethyldisiloxane occurs[24,25] via (i) primary cleavage of the Si-C and C-H bonds and (ii) subsequent splits of the Si-O bonds in intermediate products. The latter decomposition yields methane, ethene, ethane, ethyne and methylsilanes, together with a solid polyoxocarbosilane, whose formation was accounted for in terms of polymerization of transiently produced silicon-centred radicals and silanones.[26] The main plausible reactions yielding clusters of elemental iron and agglomerates of the organosilicon polymer are illustrated in a simplified Scheme 1.

The simultaneous formation of the both final products creates conditions for production of an iron–polymer

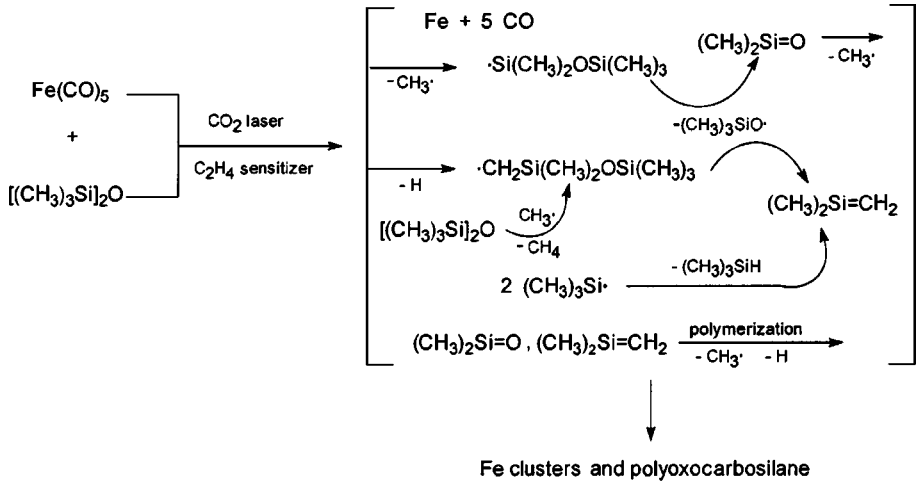

Scheme 1.

Table 2. Laser synthesis of ultrafine powders

Run	XPS analysis: Before Ar-ion sputtering	XPS analysis: After Ar-ion sputtering	Fe (wt%)	BET surface (m^2g^{-1})	Average pore diameter (nm)
1	$Si_{1.00}C_{1.38}O_{1.62}Fe_{0.16}$	$Si_{1.00}C_{0.68}O_{1.39}Fe_{0.32}$	32	94.2	8.0
2	$Si_{1.00}C_{2.54}O_{3.26}Fe_{0.83}$	$Si_{1.00}C_{2.57}O_{2.65}Fe_{4.15}$	76	51.5	8.1

composite. The analyses of the black powders obtained at the two different flow rates of hexamethyldisiloxane and iron pentacarbonyl (and different total pressures, Table 1) show that some properties of the composites (Table 2) depend on these parameters. The composite from run 1 contains less iron (is richer in organosilicon polymer) and has a higher BET surface area than that from run 2. (We note that both BET values resemble those observed for nanostructured polyoxocarbosilane[27] and polyborocarbosiloxane[28] powders prepared by similar laser-induced procedures.)

Spectral properties

The X-ray photoelectron spectra of the superficial layers reveal that both powders have similar features. The spectra of the silicon (2p) electrons can be decomposed into two components (at 102.2 and 103.4 eV) and resemble those of ultrafine polyoxocarbosilane powders obtained by laser decomposition of hexamethyldisiloxane.[25] The carbon (1s) spectra can be deconvoluted into components at 284.8, 286.7 and 289.2 eV, which are assignable[28,29] to CH_x, C–O and O=C–O moieties. The iron (2p) spectra reveal[29,30] the presence of two chemical states of iron, i.e. that of Fe^0 (707.5 eV) and Fe^{3+} (Fe_2O_3, 711.5 eV). The mild ion sputtering leads to a significant increase of total iron concentration (Table 2) and to an increase in concentration of the elemental iron (Fig. 1). This finding is consistent with elemental iron being present mostly in inner layers and Fe_2O_3 occurring in outer layers.

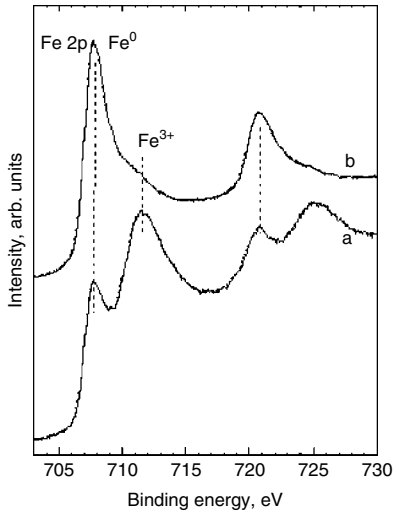

Figure 1. X-ray photoelectron spectra of the powder from run 2 before (a) and after (b) ion sputtering.

The Raman spectra of both powders in the different regions examined show a bundle of bands at 223, 289, 409 and 1316 cm^{-1} and a broad band at 690 cm^{-1} that are respectively assignable[31,32] to α- and γ-Fe_2O_3.

The FTIR spectra of both powders show a typical pattern of polyoxocarbosilanes (Fig. 2) and consist of bands at 2960–2860 cm^{-1} and ~1030 cm^{-1} that correspond to the

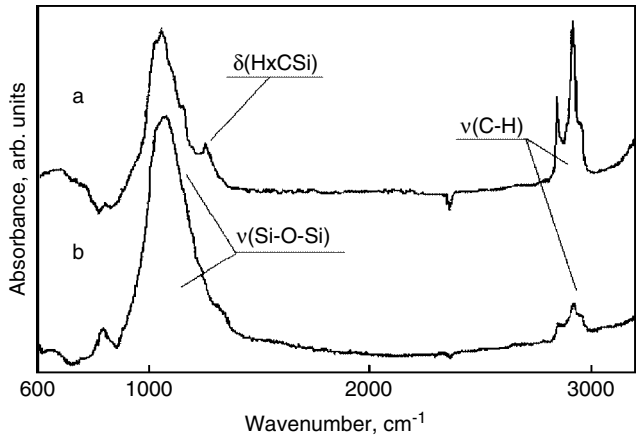

Figure 2. FTIR spectra of the powder from run 1 (a) and run 2 (b).

ν(C–H) and ν(SiOSi) stretching vibrations. The higher relative absorbance of the ν(C–H) band and the occurrence of the $\delta(CH_x)$ band at 1260 cm^{-1} for the powder from run 1 (but not for that from run 2) indicates that it has more abundant C–H bonds.

The EPR spectrum of the powder from run 1 shows a single line with *g*-factor 2.122 and a line width 95.06 mT. The total concentration of paramagnetic centres amounts to 2.2×10^{23} per gram and exceeds the possible theoretical limit (for 'high spin' ^{58}Fe it amounts 4.08×10^{22} spins per gram). Such discrepancy hints at interaction between spins, probably in superparamagnetic form.[33] The EPR spectrum of the powder from run 2 shows a featureless monotonic drift of baseline with increasing magnetic field and may be explained by ferromagnetic[34] interactions.

Electron microscopy

TEM images (Fig. 3) are compatible with cross-linked chains of ~20–50 nm in diameter which appear together with balls of ~20–100 nm in size (run 1) and with rather uniform ~20–30 nm diameter cross-linked chains (run 2). The balls consist of dark cores and a lighter shell phase that can be respectively attributed to elemental iron and a blend of iron oxide and polyoxocarbosilane. The balls in the powder from run 1 show a different thickness of the lighter shell (balls designated A and B in Fig. 3c). Conversely, the core–shell parameters in the narrow cross-linked chains do not vary and are similar, as illustrated in Fig. 3d.

Thermal properties

The thermal behaviour of the powders was examined up to 700 °C (Fig. 4). Both powders are rather stable and lose about 12% of their weight. This indicates that the powder from run 2 (possessing more iron) releases a greater fraction of the organic shell, implying that the organic shell in this powder is less stable.

The gaseous products observed are methane (main product), ethene and ethyne (traces). An interesting effect of the iron content on the progress of evolution of methane was observed (Fig. 5): the powder from run 1 (with the lower

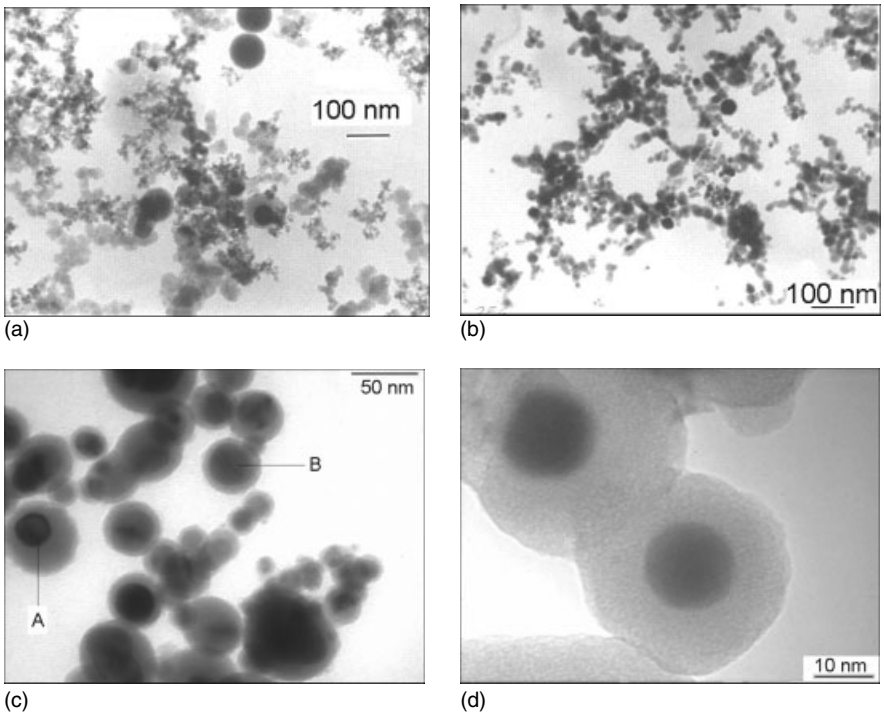

Figure 3. TEM images of the powder from run 1 (a, c, d) and run 2 (b).

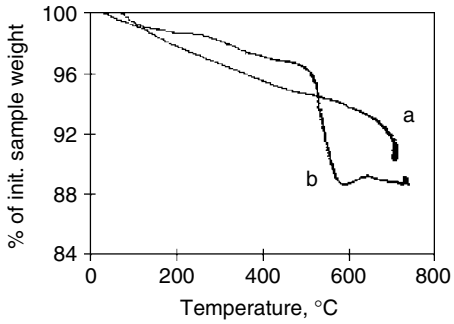

Figure 4. Thermal decomposition of the powder from run 1 (a) and run 2 (b).

Table 3. Magnetic properties of the powders

	m_0 (emu g^{-1})			H_c (Oe)		H_{ex}
Run	5 K	300 K	300 K (Fe)	5 K	300 K	(5 K) (Oe)
1	25.3	21.7	67.8	1025	77	230
2	98.3	83.7	114.7	1830	423	110

amount of iron) yields methane mostly at higher temperature (600 °C), whereas that from run 2 (with the higher amount of iron) liberates methane mostly at lower temperatures (200–400 °C). The degradation of the larger fraction of the polymer shell and the earlier evolution of methane observed for the powder from run 2 can be explained by a catalytic effect of more abundant iron. The polymeric shell formed in run 2 contains less C–H bonds (FTIR spectra, Fig. 2); therefore, it is plausible that it will be more stable than the shell formed in run 1.

Magnetic properties

The magnetic state of the samples was characterized using the measurements of the magnetization curves, hysteresis loops and AC susceptibility in the temperature range 5–400 K. These measurements yielded information on the saturation magnetization m_0 and coercivity H_c at different temperatures. (Table 3). In addition, we determined the exchange bias H_{ex} at $T = 5$ K by comparing the hysteresis loops measured in zero-field-cooled (ZFC) and field-cooled (FC) regimes between 300 and 5 K. A non-zero exchange bias indicates the presence of an iron oxide shell surrounding the iron particle.[35,36] In our case, the measured values of H_{ex} are similar to those reported, when the surface oxidation of the nanoparticles was due only to the exposure to the atmosphere.[36] A relatively larger content of oxides for sample run 1 is probably related to a larger number of small iron particles (Fig. 3).

In Table 3 we give the saturation magnetization m_0(Fe) (300 K) per weight unit of iron evaluated from the relation $m_0(\text{Fe}) = m_0/p$, where p is the weight fraction of iron from Table 2. This value is smaller than 164.5 emu g^{-1} corresponding to the bulk iron[37] as a consequence of effects at the surface of the particles.[38]

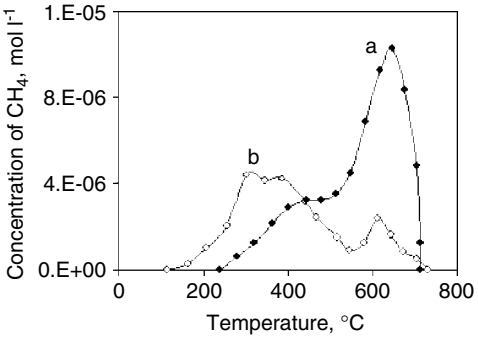

Figure 5. Concentration of methane as evolved at different temperatures from the powder from run 1 (a) and run 2 (b).

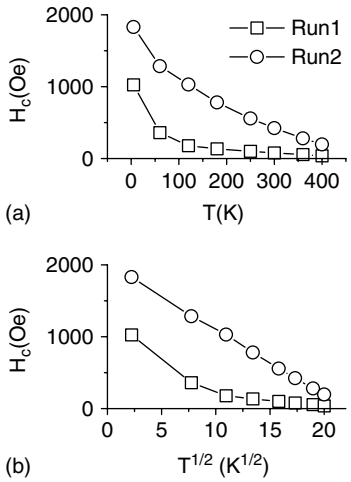

Figure 6. Coercivity as a function of (a) temperature and (b) $T^{1/2}$.

A very interesting comparison of both samples can be performed in analyzing the temperature dependence of the coercivity (Fig. 6a). It is known that for non-interacting single-domain particles H_c can be expressed as[39]

$$H_c = H_c(0)[1 - (T/T_B)^{1/2}] \quad (1)$$

where T_B is a blocking temperature and $H_c(0)$ the value of H_c for T approaching zero. If we plot H_c as a function of $T^{1/2}$, the straight-line character of this dependence (Fig. 6b) shows that only for the powder from run 2 can the experimental data be approximated by Eqn (1). In this case we obtain the parameters $T_B = 477$ K and $H_c(0) = 2030$ Oe. At first sight this result seems to be unclear, since the powder from run 2 has a larger iron content, which leads to an interaction between iron particles. The explanation of this behaviour can be found by inspecting the results of the electron microscopy analyses. The diameters D of the iron particles from the powder from run 1 were estimated to be between 20 and 100 nm, whereas for the powder from run 2 there is a rather uniform distribution

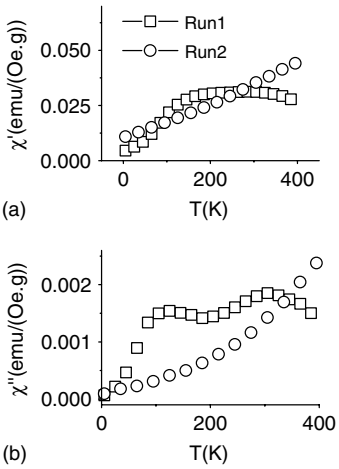

Figure 7. Real (a) and imaginary (b) parts of the AC susceptibility measured at $f = 0.3$ Hz with an exciting field of 3.9 Oe.

between 20 and 30 nm observed. Equation (1) was derived for a T_B corresponding to a definite core diameter D and cannot be applied to the complicated case of a distribution existing for sample run 1. In our case, evidently, this fact played a more important role than the influence of inter-particle interactions.

Note now the temperature dependence of the real and imaginary components of the AC susceptibility χ (Fig. 7a and b). For the powder from run 1 we observe a wide plateau between 190 and 320 K with a decrease of χ' towards higher temperatures and an interesting course of the imaginary part χ'' with two maxima at 121 and 305 K. On the other hand, both components of the susceptibility for the powder from run 2 increase with increasing temperature. A more complicated behaviour of the susceptibility for the powder from run 1 can be understood by referring to a wide distribution of the particle diameters $f(D)$. In Fig. 3, we can, for example, see nanoparticles with approximate core diameters of 15, 22.5, and 75 nm. The occurrence of the two maxima in the dependence $\chi''(T)$ for the powder from run 1 suggests, then, the possibility of the distribution $f(D)$ having two maxima. Let us recall that the largest particles are certainly in a multidomain state,[39] which manifests itself in large values of the imaginary component χ'' (domain-wall motion). In contrast to this, for the powder from run 1, smaller particles (e.g. 15 nm) can have their blocking temperatures below room temperature[40] and, being superparamagnetic, they may cause a decrease of the real component χ' observed for $T > 320$ K.

CONCLUSIONS

Continuous-wave IR laser-induced and ethylene-sensitized co-pyrolysis of gaseous iron pentacarbonyl and hexamethyldisiloxane in argon is shown as an efficient method for production of iron nanoparticles enveloped with a polymeric polyoxocarbosilane shell. The outer layers of these nanocomposites become partially oxidized upon contact with air and change into Fe–Fe_2O_3 (coreshell) nanobodies surrounded with polyoxocarbosilane. Such behaviour is indicative of incomplete coverage (protection) by the polymeric shell, or of a porous structure to the polymer.

Spectral and electron microscopy analyses of the nanocomposites obtained at two different flow rates of iron pentacarbonyl and hexamethyldisiloxane and different total pressures reveal differences in structure, thermal behaviour and magnetic properties. The iron-rich nanocomposite (which is poor in polyoxocarbosilane) has a rather uniform size of nanochains, whereas the iron-poor nanocomposite (which is richer in polyoxocarbosilane) contains both nanochains and nanoballs of various sizes. The organosilicon polymer shell in the former contains less C–H bonds. The thermal behaviour of both composites is characterized by a two-stage evolution of methane, but both stages are of different significance in each of them.

In the whole temperature region 5–400 K, both nanocomposites were found to be in a ferromagnetic blocked state with a minor superparamagnetic contribution of the smallest nanoparticles in the iron-poor nanocomposite. The exchange bias measured corresponds to the surface oxidation of the particles due to the atmosphere. For the iron-rich nanocomposite, blocked iron particles are single domain, whereas some of the large particles are in the multidomain state for the iron-poor nanocomposite. The behaviour of the coercivity and susceptibility was found to be in agreement with the results of the electron microscopy analysis. In particular, the temperature dependence of H_c for the nanocomposite rich in iron suggests the presence of single-domain particles with a blocking temperature of 477 K, and the AC susceptibility shows the possibility of a complicated distribution function $f(D)$ exhibiting two maxima.

Acknowledgements

The work was supported by NATO Collaborative Research Grant CLG 980587. We thank Dr Šolcová for BET measurements.

REFERENCES

1. Shull RD, Bennett LH. *Nanostruct. Mater.* 1992; **1**: 83.
2. Shull RD, Ritter JJ, Swartzendruber LJ. *J. Appl. Phys.* 1991; **69**: 54 144.
3. Fröba M, Köhn R, Bouffaud G, Richard O, van Tendeloo G. *Chem. Mater.* 1999; **11**: 2858.
4. Borelli NF, Morse DL, Schreurs JWH. *J. Appl. Phys.* 1983; **54**: 3344.
5. Chen L, Yang WJ, Yang CZ. *J. Mater. Sci.* 1997; **32**: 3571.
6. Kryszewski M, Jeszka JK. *Synth. Met.* 1998; **94**: 99.
7. Ziolo RF, Giannelis EP, Weinstein BA, O'Horo MP, Ganguly BN, Mehrotra V, Russell MW, Huffman DR. *Science* 1992; **257**: 219.
8. Okada H, Sakata K, Kunitake T. *Chem. Mater.* 1990; **2**: 89.
9. Petri-Fink A, Chastellain M, Juillerat-Jeanneret L, Ferrari A, Hofmann H. *Biomaterials* 2005; **26**: 2685.
10. Sohn BH, Cohen RE. *Chem. Mater.* 1997; **9**: 264.

11. Mayer CR, Cabuil V, Lalot T, Thouvenot R. *Angew. Chem. Int. Ed. Engl.* 1999; **38**: 3672.
12. Kumar RV, Koltypin Yu, Cohen YS, Cohen Y, Aurbach D, Palchik O, Felner I, Gedanken A. *J. Mater. Chem.* 2000; **10**: 1125.
13. Nustad KS, Funderud TE, Berge A, Ugelstad J. In *Scientific Methods for the Study of Polymer Colloids and their Applications*, Candau F, Ottewill RH (eds). Kluwer Academic: Dordrecht, 1990; 517.
14. Dresco PA, Zaitsev SV, Gambino RJ, Chu B. *Langmuir* 1999; **15**: 1945.
15. El-Shall MS. *Appl. Surf. Sci.* 1996; **106**: 347 and references cited therein.
16. de Caro D, Ely TO, Mari A, Chaudret B. *Chem. Mater.* 1996; **8**: 1987.
17. Pola J, Bastl Z, Vorlíček V, Dumitrache F, Alexandrescu R, Morjan I, Sandu I, Ciupina V. *Appl. Organometal. Chem.* 2004; **18**: 337.
18. Russell DK. *Chem. Soc. Rev.* 1990; **19**: 407.
19. Veintemillas-Verdaguer S, Bomati O, Morales MP, Di Nunzio PE, Martelli S. *Mater. Lett.* 2003; **57**: 1184.
20. Huisken F, Kohn B, Alexandrescu R, Morjan I. *J. Chem. Phys.* 2000; **113**: 6579.
21. Hofmeister H, Huisken F, Kohn B, Alexandrescu R, Cojoraru S, Cruntenanu A, Morjan I, Diamandescu L. *Appl. Phys. A* 2001; **72**: 7.
22. Bomati Miguel O, Morales MP, Serna CJ, Veintemillas-Verdaguer S. *IEEE Trans. Magn.* 2002; **38**: 2616.
23. Veintemillas-Verdaguer S, Morales MP, Serna CJ. *Appl. Organometal. Chem.* 2001; **15**: 365.
24. Manders WF, Bellama JM. *J. Polym. Sci. Polym. Chem. Ed.* 1985; **23**: 351.
25. Kupčík J, Bastl Z, Šubrt J, Pola J, Papadimitriou VC, Prosmitis AV, Papagiannakopoulos P. *J. Anal. Appl. Pyrol.* 2001; **57**: 109.
26. Pola J, Galíková A, Galík A, Blechta V, Bastl Z, Šubrt J, Ouchi A. *Chem. Mater.* 2002; **14**: 144.
27. Pola J, Tomovska R, Barkadjieva S, Galíková A, Vacek K, Galík A. *J. Non-Cryst. Solids* 2003; **328**: 227.
28. Pola J, Herlin-Boime N, Brus J, Bastl Z, Vacek K, Šubrt J, Vorlíček V. *Solid State Sci.* 2005; **7**: 123.
29. NIST X-ray Photoelectron Spectroscopy Database, ver. 2.0. US Department of Commerce, NIST, Gaithersburg, MD, USA, 1997.
30. Tan BJ, Klabunde KJ, Sherwood PM. *Chem. Mater.* 1990; **2**: 186.
31. Oblonsky LJ, Devin TM. *Corros. Sci.* 1995; **37**: 17.
32. De Faria DLA, Silva SV, de Oliveira MT. *J. Raman Spectrosc.* 1997; **28**: 873.
33. Hseih CT, Huang WL, Lue JT. *J. Phys. Chem. Solids* 2002; **63**: 733.
34. Griscom DL, Friebelle EJ, Shinn DB. *J. Appl. Phys.* 1979; **50**: 2402.
35. Kiwi MJ. *Magn. Magn. Mater.* 2001; **234**: 584.
36. Baker C, Ismat Shah S, Hasanain SK. *J. Magn. Magn. Mater.* 2004; **280**: 412.
37. Burke NAD, Stover HDH, Dawson FP. *Chem. Mater.* 2002; **14**: 4752.
38. Gangopadhyay S, Hadjipanayis, Dale B, Sorensen CM, Klabunde J, Papaefthymiou V, Kostikas A. *Phys. Rev. B* 1992; **45**: 9778.
39. Cullity BD. *Introduction to Magnetic Materials*. Addison-Wesley: 1972.
40. Wilson JL, Poddar P, Frey NA, Srikanth H, Mohomed K, Harmon JP, Kotha S, Wachsmuth J. *J. Appl. Phys.* 2004; **95**: 1439.